This paper appears in IEEE Transactions on Biomedical Engineering, 2016.
DOI: 10.1109/TBME.2016.2565690

A Hand-Held Assistant for Semi-Automated Percutaneous Needle Steering

Carlos Rossa, Nawaid Usmani, Ronald Sloboda, and Mahdi Tavakoli

***Abstract*—*Objective*: Permanent prostate brachytherapy is an effective and popular treatment modality for prostate cancer in which long needles are inserted into the prostate. Challenges associated with manual needle insertion such as needle deflection limit this procedure to primarily treat the entire prostate gland even for patients with localized cancer. In this paper we present a new semi-automated hand-held needle steering assistant designed to help surgeons improve needle placement accuracy. *Methods*: Regular clinical brachytherapy needles are connected to a compact device that the surgeon holds. As the surgeon inserts the needle, the device rotates the needle base on a measured and calculated basis in order to produce a desired trajectory of the needle tip. A novel needle-tissue interaction model and a steering algorithm calculate such control actions based on ultrasound images of the needle in tissue. The assistant can also apply controlled longitudinal microvibrations to the needle that reduce needle-tissue friction. *Results*: Experimental validation of the proposed system in phantom and *ex-vivo* biological tissue report an average needle targeting accuracy of 0.33 mm over 72 needle insertions in 12 different experimental scenarios. *Conclusion*: We introduce a new framework for needle steering in prostate brachytherapy in which the surgeon remains in charge of the needle insertion. The device weighs 160 grams, making it easy to incorporate with current insertion techniques. *Significance*: Expected benefits of the proposed system include more precise needle targeting accuracy, which can result in improved focal treatment of prostate cancer.**

***Index Terms*—Needle insertion, medical device, prostate brachytherapy, steerable needles, robotic assistance.**

I. INTRODUCTION

ONE out of eight Canadian men and one in six American men will be diagnosed with prostate cancer during their lifetime [1], [2]. In Canada, prostate cancer accounts for roughly one-quarter of all cancer cases in men, making it the leading cause of cancer deaths with 24,000 diagnoses and 4,100 deaths in 2015 [1].

Permanent brachytherapy using radioactive seeds is an efficacious treatment for prostate cancer due to its excellent success rates, favourable toxicity profile, and non-invasiveness [3]. This procedure delivers radiation to tumours by implanting radioactive seeds in close proximity to the tumour or within the tumour itself by means of long hollow, seed-carrying needles. Despite good clinical outcomes, close scrutiny of the technical aspects of prostate brachytherapy indicates that there is considerable room for improvement. A major challenge that can compromise the quality of an implant is the inadvertent placement of seeds due to deflection of the needle and tissue displacement, both of which are difficult to control during manual needle insertion. Previous studies have shown that seeds are placed with an average absolute accuracy of 5 mm, a substantial error of more than 10% of the average prostate diameter [4].

Because of insufficient seed placement accuracy, current brachytherapy practice is limited to treating the entire prostate gland uniformly even for patients with only localized prostate cancer. Instead, to move away from treating the entire prostate and target specific areas of dominant tumours, delivering higher radiation doses to these targeted areas using seeds can be considered [5]. This has generated a need for improved needle steerability and targeting accuracy, which is essential to minimizing the risk of undesired radiation exposure to adjacent healthy tissues.

In an effort to improve needle targeting accuracy, several researchers have implemented full-fledge robotic systems to automatically insert a needle in tissue and undertake the necessary corrective actions to control its trajectory towards a target. To create the steering effect, these systems generally rely on a key observation that when a bevelled-tip needle is pushed into tissue an imbalance of forces is created at the needle tip causing it to bend. Rotating the needle base to change the orientation of the bevel and consequently the direction of the resultant force is then used to control the direction of needle deflection [6]. Among the first robotic systems for needle steering, a fully automated biopsy system with computed tomography is presented in [7]. Smith *et al.* [8] have developed a similar apparatus combined with real-time ultrasound. In [9], a robotic arm with active translational motion for percutaneous renal access is reported. A robotic system introduced in [10] uses a seven degrees-of-freedom, passive mounting arm and a motorized needle-insertion device to deliver 18-gauge implant needles into the prostate. Along the same line, a needle insertion device for seed implantation in the prostate under ultrasound image guidance is developed in [11]. In [12], a system for intra-tumoural placement of drugs uses intraoperatively acquired computer tomographic images for guidance of needles. Based on these images, the physician selects an appropriate tumour target and plans the instrument's

This work was supported in part by the Natural Sciences and Engineering Research Council of Canada (NSERC) under grant CHRP 446520, in part by the Canadian Institutes of Health Research (CIHR) under grant CPG 127768, and in part by Alberta Innovates - Health Solutions (AIHS) under grant CRIO 201201232.

C. Rossa and M. Tavakoli are with the Department of Electrical and Computer Engineering, University of Alberta, Edmonton, AB, T6G 2V4, Canada (e-mail: rossa@ualberta.ca; madhi.tavakoli@ualberta.ca).

N. Usmani and R. Sloboda are with the Cross Cancer Institute and the Department of Oncology, University of Alberta, Edmonton, AB, T6G 1Z2, Canada (e-mail: nawaid.usmani@albertahealthservices.ca; ron.sloboda@albertahealthservices.ca).

trajectory. The robot subsequently drives the instrument to the desired location. These are only a few examples of robotic needle insertion devices; we refer the reader to [13] for a complete survey.

Despite many advantages offered by robotic needle steering, i.e., high accuracy, repeatability, and reliability, such systems have not yet been widely adopted in clinical practice. This is partially due to the significant modifications that would be necessary in the operating room in order to implement such fully automated needle insertion systems. Likewise, due to the lack of accurate needle deflection feedback, needle steering in terms of calculated rotation of the needle base is generally not manually performed by surgeons [14]. An intermediate solution to bring needle steering into clinical practice can be sought in providing oncologists with a higher degree of control over the needle insertion trajectory without modifying the clinical procedure.

In this paper we introduce the first hand-held needle insertion assistant dedicated to seed implantation during prostate brachytherapy (see Fig. 1(a) and the attached video). The assistant system is designed to assist surgeons to enhance needle targeting accuracy by *automatically* rotating the needle at appropriate insertion depths as the surgeon *manually* inserts it. In contrast to existing fully-automated needle insertion systems, for safety and clinical acceptance reasons, in the approach presented here the surgeon remains in charge of the needle insertion and the proposed device will not modify neither the operating room setup nor the current brachytherapy practice. The proposed system uses ultrasound images of the needle in tissue and a needle-tissue interaction model to predict future needle deflections during insertion. A needle steering algorithm calculates the insertion depth(s) at which the needle must be rotated to ensure that the needle tip reaches a desired destination. The device is also able to vibrate the needle axially in a controlled manner in order to reduce friction between the needle shaft and the tissue and make the insertion easier for the surgeon. The device weighs 160 grams, making it easy to incorporate with current insertion techniques. The proposed framework for semi-automated needle insertion into prostate is novel. The only similar work consists of a device for biopsy presented in [15] that, unlike our system, uses an extensible curved stylet inserted in the needle shaft to control the needle trajectory, and a system for hand-held manipulation of an endoscope and a concentric tube that was presented in [16].

We present a comprehensive needle steering assistant composed of three complementary parts as schematically depicted in Fig. 2: 1) a needle insertion device, 2) an algorithm that estimates the needle deflection as the needle is inserted, and 3) a needle steering planning subsystem. These will be described in sections II to IV. In Section V we present the experimental setup used to validate the proposed system. Experimental results performed in phantom and *ex-vivo* biological tissue reported in Section VI confirm the suitability of the proposed semi-automated system for assisted needle steering.

Contributions of this paper include the novel design of a compact and fully hand-held device that is compatible with routine brachytherapy needles currently used in clinical practice. The proposed design allows the needle-carrying seeds to be simultaneously rotated axially and vibrated longitudinally. Another contribution presented here is the image-based identification of the needle-tissue model parameters and the needle steering controller that works in tandem with the needle steering apparatus.

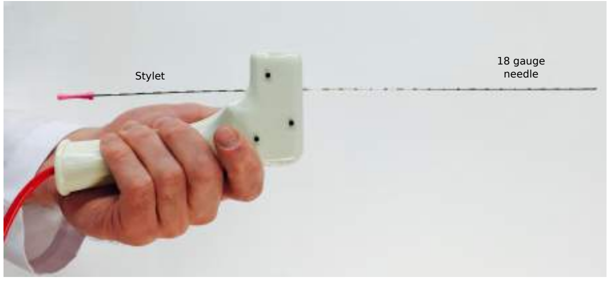

(a) The prototype steering assistant

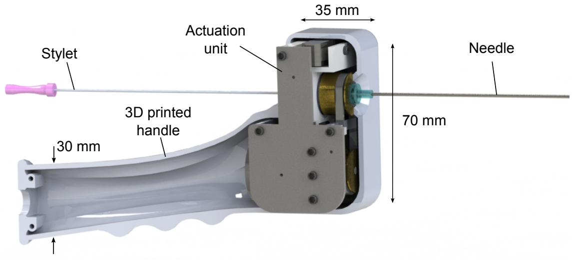

(b) CAD cross sectional view

Fig. 1. The needle steering assistant for semi-automated needle insertion (a). As the surgeon pushes the device and the needle, the device automatically rotates the needle axially at appropriate positions in order to reach a desired target. Longitudinal vibrations can be applied to the needle in order to reduce needle-tissue frictional forces. In (b) the CAD cross-sectional view of the apparatus shows the embedded actuation unit.

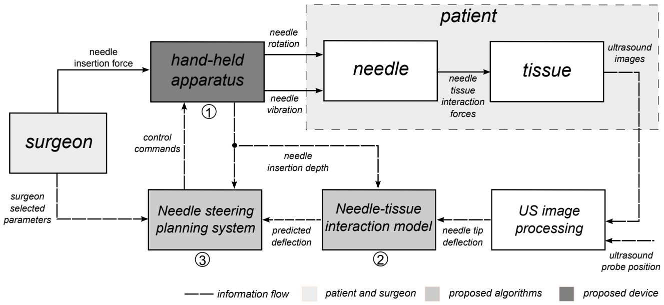

Fig. 2. Different parts that comprise the proposed needle steering system: the hand-held apparatus, the needle-tissue interaction model, and the needle steering planning system.

II. THE HAND-HELD ASSISTANT

Fig. 1(b) shows a cross section of the proposed needle assistant. It is composed of a compact actuation unit for axial needle rotation, to which a standard 18-gauge hollow brachytherapy needle is connected, and a 3D printed handle that the surgeon holds. The inner workings of the actuation unit are detailed in Fig. 3. As the surgeon pushes the device toward the patient, the actuation unit can rotate the needle shaft axially and apply controlled longitudinal vibrations to the needle. As in fully manual brachytherapy, a stylet is inserted in the needle shaft. Once the target depth is reached, the surgeon keeps the stylet in place and retracts the device (and the needle) such that the stylet deposits the seeds from inside the needle into the prostate.

Needles used in brachytherapy often have a standard bevelled tip. As the needle tip cuts through tissue, tissue displacement at the edge of the bevel creates a resultant force normal to the needle shaft that causes it to bend on a curved trajectory. Hence, changing the orientation of the bevel angle via axial rotation of the needle base changes the direction of the force applied at the needle tip, causing the needle to bend in a different direction. Thus, a proper combination of needle translation and axial rotation can force the needle tip to follow a desired trajectory [17], [18], [19], [20], [21], [22], [23].

To allow for axial rotation of the needle, the needle's base connects to a threaded holder actuated by a DC motor (model 26195024SR from Faulhaber, Croglio, Switzerland) through a miniature timing belt and pulley mechanism (see Fig. 3a). A rigid hollow shaft links the needle holder to the housing using two low friction ball bearings (see the exploded view shown in Fig. 3(b)). This allows the stylet to be inserted into the needle shaft from the other side of the needle holder. The motor has embedded reduction gears with a 33:1 reduction ratio. An incremental encoder with 16 pulses per revolution connected to the gears measures the axial position of the needle shaft with 0.1 degree accuracy. The motor is powered by a L298N PWM drive and a computer-implemented PID controller calculates the required PWM duty cycle in order to control the angular position of the needle shaft.

The needle holder and housing assembly slides on two miniature linear rails such that they can translate horizontally in the direction of insertion. In order to allow for simultaneous needle rotation and some small longitudinal relative translation of the pulleys, a 2 mm clearance is added to the length of the timing belt. A supporting structure and the linear rails are then connected to two opposite lateral walls (only one is shown in Fig. 3).

In order to generate a controlled horizontal displacement of the housing (and of the needle), an amplified piezoelectric actuator (APA60S from Cedrat Technologies, Meylan, France) applies high-frequency micro-vibrations of less than 40 μm in amplitude to the housing. The piezoelectric actuator converts an electrical signal into a very small displacement, making the device intrinsically safe and the vibrations virtually undetectable by the surgeon. The piezoelectric actuator is powered by a piezoelectric drive (PDm200, PiezoDrive, Callaghan, Australia). Note that the housing cannot be moved on the linear rails when the piezoelectric actuator is turned off. The reason for using axial needle vibration is that translational friction along the needle shaft can be reduced by modulating a vibratory low-amplitude displacement onto a regular needle insertion profile [24]. These very low amplitude vibrations are undetectable by the surgeon and make the needle insertion and withdrawal easier.

The compact actuation unit is placed in a 3D printed handle. In order to track the position of the handle in real time, the 3D position of tracking markers added to its left is measured at 20 Hz by a dual camera optical motion tracker (BB2-BW-Hx60 from Claron Tech, Toronto, Canada).

In the next section, we present the needle-tissue interaction model that will be used to calculate the depths at which the device must rotate the needle as the surgeon pushes it into tissue, such that a desired needle tip trajectory can be achieved.

III. NEEDLE-TISSUE INTERACTION MODEL

The first step in calculating the depth of needle rotation requires modelling the needle-tissue interaction in order to predict future needle deflection. The objective here is to develop a model that can be entirely identified using only 2D ultrasound images of the needle in tissue, which are often available in clinical settings. In prostate brachytherapy, the needle ideally follows a straight line trajectory. Hence, and as there is no need to generate 3D trajectories, we will limit the model to capture planar needle deflections.

The needle is modelled as a cantilever compliant beam that undergoes forces applied by the tissue. According to the Galerkin-Bubnov method [25], beam deflection can be approximated as the sum of n candidate shape functions (eigenfunctions), each of which represents a mode of vibration. The deflection $v(d,z)$ of a needle at a point z along its shaft and, for a given insertion depth d in our case, can be defined as [26], [27]

$$v(d,z) = \sum_{i=0}^{n} q_i(z) g_i(d), \tag{1}$$

where $q_i(z)$ is the displacement of the needle (deflection) at each point z along its shaft and $g_i(d)$ is a weighting coefficient (eignenvalue) for each of the n assumed vibration modes. The eingenfunctions $q_i(z)$ must satisfy the boundary conditions of a cantilever beam and be differentiable at least up to the highest order of the partial differential equations of the beam. For a cantilever beam of length L, the deflection can be given by [25]

$$q_i(z) = \frac{1}{\kappa_i}\left[\sin\xi(z) - \sinh\xi(z) - \gamma_i\left\{\cos\xi(z) - \cosh\xi(z)\right\}\right] \tag{2}$$

where

$$\xi(z) = \beta_i \frac{z}{L} \tag{3}$$

and the constants γ_i and κ_i are computed as

$$\begin{aligned} \gamma_i &= \frac{\sin\beta_i + \sinh\beta_i}{\cos\beta_i + \cosh\beta_i} \\ \kappa_i &= \sin\beta_i - \sinh\beta_i - \gamma_i(\cos\beta_i - \cosh\beta_i). \end{aligned} \tag{4}$$

The values of the constants β_i for a clamped-free beam are $\beta_1 = 1.857$, $\beta_2 = 4.695$, $\beta_3 = 7.855$, $\beta_4 = 10.996$, and $\beta_i \simeq \pi(i - 1/2)$ for $i > 4$ [25]. At this stage the assumed displacement functions are entirely parametrized. In the following, we demonstrate that the weighting coefficients $g_i(d)$ can be given as functions of the needle-tissue interaction forces such that the system reaches equilibrium.

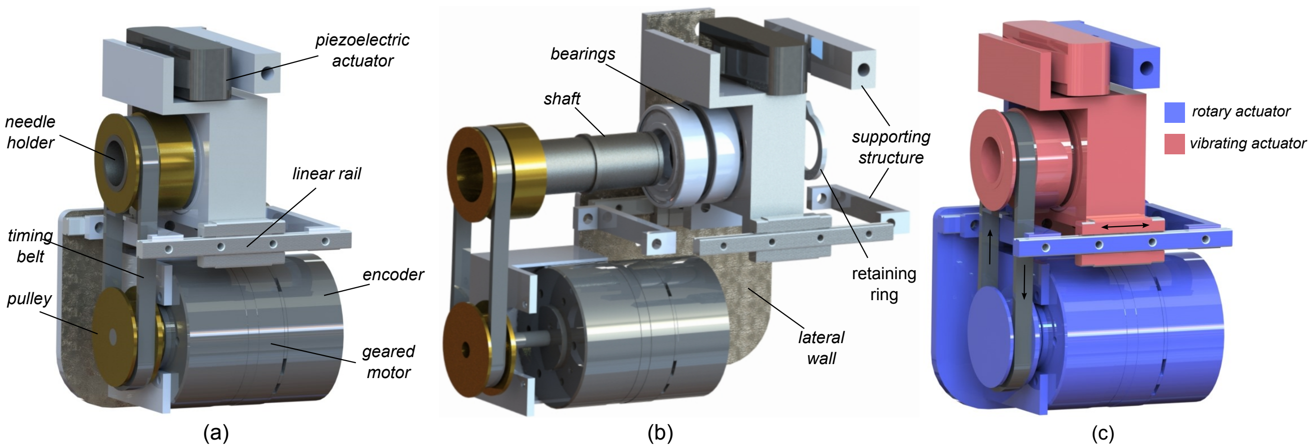

Fig. 3. Inner workings of the needle assistant actuation unit. The different parts that make up the system are labelled in (a). The exploded view of (a) is shown in (b), demonstrating the mechanical structure that allows for axial rotation and longitudinal vibration of the needle. In (c), the longitudinal vibration actuator (red) and the axial rotation actuator (blue) are highlighted.

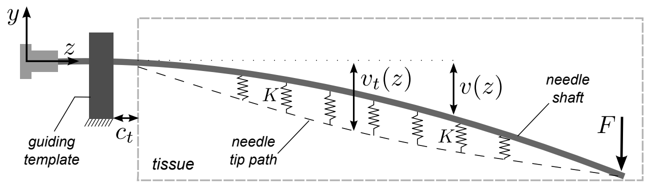

Fig. 4. Needle insertion in soft tissue using a guiding template. As the needle cuts a path in the tissue, a force F is applied to the needle tip causing the needle to bend. Tissue compression as a result of needle deflection is assumed to be the difference between the current shape of the needle $v(z)$ and the path cut by the needle tip $v_t(z)$. c_t is the distance between the grid template and the tissue.

A. Needle-Tissue Equilibrium

The Rayleigh-Ritz method and the principle of minimum potential energy are used to calculate the weighting coefficients $g_i(d)$ that bring the system to equilibrium. This approach has been previously employed to estimate needle deflection in [27], [20]. Here, we propose a novel tissue model that accepts unlimited number of needle rotations while accounting for tissue displacement. In addition, we report a mathematical approach that reduces the model to a simple system of linear equations, making it computationally efficient, and enabling it to be identified using only ultrasound images of the needle during insertion.

The coefficients $g_i(d)$ must minimize the system potential $\Pi(d)$ defined by

$$\Pi(d) = U(d) + V(d) \tag{5}$$

where $U(d)$ is the total stored energy in the system and $V(d)$ is the work done by conservative forces. Let us now derive the expressions for the potential energy and the work for the needle-tissue system.

As the needle tip cuts through the tissue, the bevel creates a resultant force F at the needle tip (see Fig. 4). We will neglect other forces applied at the tip as they mostly induce axial compression of the needle. As the needle bends, the work due to F is

$$V(d) = -Fv(d, L). \tag{6}$$

The bending strain energy stored in the needle as a result of deflection is

$$U_b(d) = \frac{1}{2}\int_0^L EI\left(\frac{\partial^2 v(d,z)}{\partial z^2}\right)^2 dz, \tag{7}$$

where E and I are the needle Young's modulus of elasticity and its second moment of inertia, respectively.

In brachytherapy, the needles are inserted through a guiding template to help guide the needle towards a target and to minimize deflection outside the tissue. We model the template as a rigid spring of stiffness $K_p >> 0$, which has no thickness. The spring is connected to the needle shaft at a distance of z_t from the needle's base with $z_t = L - d - c_t$, where c_t is the distance from the template to the tissue surface (see Fig. 4). The potential energy stored in the template is

$$U_p(d) = \frac{1}{2}K_p v(d, z_t)^2. \tag{8}$$

As the needle bends, the shaft moves and deforms the surrounding tissue. In turn, the compressed tissue applies forces to the needle shaft. Assuming small local magnitude and deformation velocity of the tissue, it is reasonable to assume that the tissue is a purely elastic medium. Thus, the force applied to the needle at a certain point along the shaft becomes proportional to the tissue displacement at that point. If we call $v_t(z)$ the initial position of the uncompressed tissue, the tissue reaction force is $K(v(d,z) - v_t(z))$, where K is the stiffness of the tissue per unit length of the needle and $v_t(z)$ is the historical position of by the needle tip. Therefore, the energy due to tissue compression is

$$U_t(d) = \frac{1}{2}K\int_{L-d}^{L}[v(d,z) - v_t(d,z)]^2 dz \tag{9}$$

B. Calculating the Eigenvalues $g_i(d)$

Now that we have defined all the components of the system potential $\Pi(d)$, we can calculate the weighting coefficients $g_i(d)$ using the principle of minimum potential energy. According to the Rayleigh-Ritz method [28], the coefficients $g_i(d)$ must give $\delta\Pi_i = 0$ for any values of δg_i where δ denotes infinitesimal difference. Therefore, $g_i(d)$ must satisfy:

$$\frac{\partial \Pi_i(d)}{\partial g_i(d)} = \frac{\partial}{\partial g_i(d)}(U_b + U_p + U_t + V) = 0 \tag{10}$$

Replacing (6)-(9) in (10) and taking the partial derivative with respect to $g_i(d)$ yields

$$\begin{aligned} &EI \int_0^L \left(\sum_{i=1}^{n} \ddot{q}_i(z) g_i(d) \right) \ddot{q}_i(z) dz \\ &+ K_p \left(\sum_{i=1}^{n} q_i(z_t) g_i(d) \right) q_i(z_t) \\ &+ K \int_{L-d}^{L} \left(\sum_{i=1}^{n} q_i(z) g_i(d) \right) q_i(z) dz \\ &- K \int_{L-d}^{L} v_t(d,z) q_i(z) dz = F, \end{aligned} \tag{11}$$

where the double dot denotes the second derivative of $q_i(z)$ with respect to z.

In order to isolate the weighting coefficients $g_i(d)$ in the previous equation, let us create four supplementary variables that we define as follows

$$\begin{aligned} \psi_{ji} &= \int_0^L \ddot{q}_i(z)\ddot{q}_j(z) dz, \qquad & \omega_{ji} &= \int_{L-d}^{L} q_i(z) q_j(z) dz, \\ \gamma_{ji} &= q_i(z_t) q_j(z_t), & \phi_i &= \int_{L-d}^{L} v_t(d,z) q_i(z) dz. \end{aligned} \tag{12}$$

After some straightforward manipulation, (11) rearranges as

$$\sum_{j=1}^{n} [\boldsymbol{g_j(d)}(EI\psi_{ji} + K\omega_{ji} + K_p\gamma_{ji})] - K\phi_i = F \tag{13}$$

This equation shows that we have reduced the model to a system composed of n linear equations. This is the closed form solution through which the coefficients $g_i(d)$ are found in order to calculate the needle deflection given in (1).

C. Tip Force Estimator

The proposed model requires only two input parameters, i.e., the tissue stiffness K and the force at the needle tip F. The first one can be obtained experimentally by model fitting and can be considered to be constant throughout the insertion. To identify the second parameter, we propose a method to estimate the force F as the needle is inserted. To this end, let us assume that the deflection of the needle tip can be acquired from ultrasound images of the needle in tissue, that we will refer to as v_L. Therefore, from (1), and knowing that $q_i(L) = 1 \ \forall i$, it yields:

$$v(L,d) = g_1(d) + g_2(d) + \dots g_n(d) = v_L \tag{14}$$

Now, adding this equation to the system of n equations given in (13) results in a system of $n+1$ expressions with only one unknown parameter (i.e., the tissue stiffness K). Hence, the coefficients $g_i(d)$ and the force applied at the needle tip at every insertion depth d are given by combining (13) and (14) to form the new system of equations expressed in matrix form as follows

$$\begin{bmatrix} g_1(d) \\ \vdots \\ g_n(d) \\ F \end{bmatrix} = \frac{K\Phi}{EI\Psi + K\Omega + K_p\Gamma + \Lambda} \tag{15}$$

where the matrices Φ, Ω, Γ, Φ and Λ are

$$\Psi = \begin{bmatrix} \psi_{11} & \dots & \psi_{1n} & 0 \\ \vdots & \ddots & \vdots & \vdots \\ \psi_{n1} & \dots & \psi_{nn} & 0 \\ 0 & \dots & 0 & 0 \end{bmatrix} \qquad \Omega = \begin{bmatrix} \omega_{11} & \dots & \omega_{1n} & 0 \\ \vdots & \ddots & \vdots & \vdots \\ \omega_{n1} & \dots & \omega_{nn} & 0 \\ 0 & \dots & 0 & 0 \end{bmatrix}$$

$$\Gamma = \begin{bmatrix} \gamma_{11} & \dots & \gamma_{1n} & 0 \\ \vdots & \ddots & \vdots & \vdots \\ \gamma_{n1} & \dots & \gamma_{nn} & 0 \\ 0 & \dots & 0 & 0 \end{bmatrix} \qquad \Lambda = \begin{bmatrix} 0 & \dots & 0 & -1 \\ \vdots & \ddots & \vdots & \vdots \\ 0 & \dots & 0 & -1 \\ 1 & \dots & 1 & 0 \end{bmatrix}$$

$$\Phi = \begin{bmatrix} \phi_{11} & \dots & \phi_{n1} & v_L \end{bmatrix}$$

Notice that all matrices but Φ in the previous equation are $n+1$ square defined. Now, needle deflection can be calculated for every insertion depth using (1).

IV. NEEDLE STEERING CONTROLLER

Here we will develop an algorithm based on the model described in the previous section to determine the depth(s) at which the needle must be rotated by the hand-held device in order to reach a desired target. The steering algorithm works in three distinct phases as follows.

Phase 1 - Observation phase: The ultrasound probe has moved in synchrony with the needle tip up to a certain insertion depth d enabling the model to predict both the needle deflection and the force applied at the needle tip F' using (15). At this stage, the current needle shape, the estimated F', and the path cut in the tissue by the needle tip are known. This information is used in Phase 2 in order to predict the needle deflection as the needle is inserted further into tissue.

Phase 2 - Prediction phase: Unlike in Phase 1, for causality reasons the force applied at the needle tip cannot be directly observed, nor can any image feedback be obtained. Therefore, in order to calculate future needle deflections from the current depth up to the target depth, we use (13) and set $F = F'u(d)$, with F' being the average estimate from Phase 1. $u(d)$ is an auxiliary variable used to reverse the orientation of the tip force when the needle base is axially rotated by 180 degrees at a depth d_r, and is given by

$$u(d) = H(d) + 2\sum_{r=1}^{N}(-1)^r H(d - d_r) \tag{16}$$

with $H(d)$ being the Heaviside step function, and N number of admissible axial needle rotations. In order to minimize tissue trauma and heating, we will limit the number of allowed axial rotations to $N = 2$ throughout this paper. As shown in Fig. 5(a), $u(d) = 1$ indicates that the needle bevel tip is facing up, causing the needle to deflect downward (as shown in Fig. 4), and $u(d) = -1$ indicates the bevel angle is facing down, leading the needle to deflect upwards. The sign of the tip force F is then reversed every time the needle passes through a depth d_r, with $1 \leq r \leq N$ and $r \in \mathbb{N}$.

Phase 3 - Control phase: Now, the role of the steering algorithm is to find the N needle rotation depths d_r that minimize a cost function J representing the total needle targeting error relative to the desired target/trajectory. For formulating J, let us consider two different procedures commonly used in permanent brachytherapy seed implantation.

Case 1: In this experimental scenario the needle is loaded with a single radioactive seed, which must be deposited at a certain target depth in tissue called d_f. Thus, the needle tip should reach the target regardless of what trajectory the needle tip takes. This case can also be considered for tissue biopsy. Since in brachytherapy the needle insertion point and the target are typically on the same horizontal line, the cost function essentially amounts to minimizing the needle tip deflection at the depth of the target (see Fig 5(b)). Hence, the cost function is

$$J_1 = |v(d_f, L)|. \tag{17}$$

Case 2: As in current low-dose rate (LDR) brachytherapy, several seeds spaced appropriately can be loaded in the same needle prior to insertion. Once the needle reaches the target depth d_f, the surgeon holds the stylet in place and withdraws the needle such that all the seeds are deposited along the prostate length, which we denote by ℓ. Ideally and according to the dosimetry pre-planning assumptions, this chain of seeds will wind up on the horizontal line that connects the target depth to the insertion point in tissue. Thus, the cost function is the mean absolute error of tip deflection inside the prostate (see Fig 5(c)). Hence, in this case we defined the cost function J_2 as

$$J_2 = \frac{1}{\ell} \sum_{d=d_f-\ell}^{d=d_f} |v(d, L)|. \tag{18}$$

The optimal depths d_r at which the device must rotate the needle are those that minimize the cost function for each scenario over a fixed control horizon. Inspired by Model Predictive Control (MPC) theory [6], the control horizon is defined as a moving window that starts at the current insertion depth and ends at a pre-defined future depth (35 mm ahead). This will correspond to the spatial interval in which the optimization solver tries to minimize the cost function. Thereby, we convert the N-variable optimization problem into a single variable optimization problem. Optimization is performed by a simulated annealing algorithm [29]. This solver provides a fast minimization of a quadratic function subject to linear and nonlinear constraints and bounds.

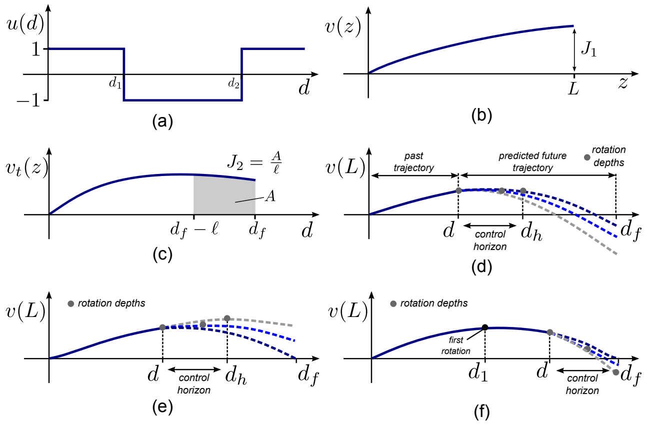

Fig. 5. Control variable $u(d)$ as a function of the needle rotation depth d_r (a), and the cost functions J penalizing needle targeting error for Case 1 (b) and Case 2 (c). Hypothetical examples of candidate rotation points within the control horizon [d,d_h] and the resultant deflection in [d, d_f] are shown in (d), (e) and (f).

Fig. 5(d) shows a hypothetical example for Case 1, where the needle is first inserted to a depth d. The controller evaluates the future needle deflection up to the target depth d_f for different rotation depth candidates sitting within the control horizon $[d, d_h]$, where $d_h = d + 35$ mm. In the current control horizon, the optimal depth for rotation is determined by the controller to be d_h. In Fig. 5(e), the needle is further advanced into tissue. Whenever the updated optimal rotation depth becomes equal to the current insertion depth, as shown in Fig. 5(f), the needle must be rotated.

The optimal rotation depths calculated using the proposed algorithm for an 18-gauge standard brachytherapy needle (whose characteristics will be given in the next section) inserted in different tissues with stiffness per unit length K ranging from 0.1×10^5 to 10×10^5 Nm^{-2} and experiencing a force at the tip of $0.1 \leq |F| \leq 3.5$ N are presented in Fig. 6. In Fig. 6(a) and Fig. 6(b), the target is a single point that is at a depth of 150 mm and 130 mm, respectively (Case 1). These results indicate that a single needle rotation is required to minimize J_1 and reach the target. For Case 2, the model predicts that two rotations are necessary to minimize the cost function J_2. The corresponding depths of the first (d_1) and second (d_2) rotations are shown in Fig. 6(c) and Fig. 6(d), for a target depth of 150 mm.

In the next section, we will implement the steering algorithm to test the proposed steering system in phantom and *ex-vivo* biological tissue.

V. HARDWARE IMPLEMENTATION AND EXPERIMENTAL SETUP

The experimental setup used to test the prototype system is shown in Fig. 7(a). The needle is inserted by the hand-held assistant into a piece of tissue held in a transparent container through a standard brachytherapy template grid (model D0240018BK, C.R. Bard, Covington, USA). The template grid prevents change in the needle insertion angle due to needle bending outside the tissue. The grid template is assumed to have a stiffness of $K_p = 10^9$ Nm^{-1}. From the measured

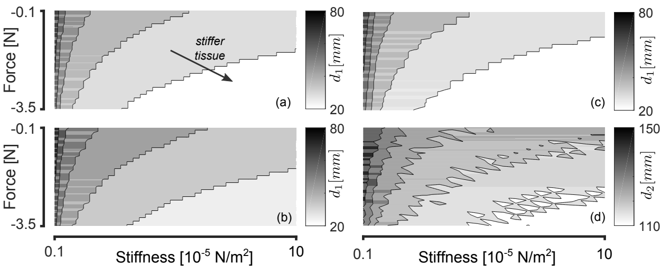

Fig. 6. Optimal rotation depth (mm) as a function of the force applied at the needle tip F and needle-tissue stiffness K. (a) and (b) show the optimal rotation depth for Case 1 for $d_f = 130$ and $d_f = 150$ mm respectivelly. In (c) and (d), the depth of first (d_1) and second (d_2) rotation that minimizes the cost function for Case 2 for $d_f = 150$ mm are presented.

position of the tracking markers and knowing the length of the needle, the needle insertion depth is deduced. The needle used throughout the experiments is a 200 mm long 18-gauge standard brachytherapy needle (Eckert & Ziegler Inc., Oxford, USA) with a Young's modulus of 200 GPa and a moment of inertia of 7.75×10^{-14} m^4.

As the needle is inserted in the tissue, a 4DL14-5/38 linear ultrasound probe connected to a Sonix Touch ultrasound machine (Ultrasonix, Richmond, Canada) slides above the tissue to acquire at 30 Hz transverse 2D ultrasound images of the needle. Transverse images show a cross section of the needle ensuring that the problem of probe alignment found in longitudinal (sagittal) imaging will not be present [19]. A linear stage motorized by a DC motor moves the ultrasound probe, while its absolute position is measured by a linear potentiometer (LP-250FJ from Midori Precisions, Tokyo, Japan) in real time (not visible in Fig. 7(a)). The ultrasound imaging plane is initially placed close to the needle tip. As the needle is pushed into the tissue, the motorized linear stage controlled by a discrete PID controller moves in synchrony with the needle tip such that the same point of the needle shaft is always visible in the image. In each image, the needle appears as a bright, elliptical object. Before the needle insertion begins, the insertion location is manually identified in the image, which automatically creates a region of interest centred around the needle's insertion location. Next, we apply contrast stretching and an intensity threshold to identify candidate pixels and use a Kalman filter to remove outliers from the region of interest, such as air bubbles and other artifacts. The Kalman filter predicts where the needle should be within the region of interest given the needle tip's historical trajectory. Once the needle is found, the region of interest is repositioned around the updated needle position estimate. The complete algorithm is described in [30].

For safety reasons, the motorised linear stage that translates the ultrasound probe is only activated when the needle is inserted through the grid template. This is achieved by establishing a virtual workspace defined as a 3D rectangular volume located in front of the grid template. For the hand-held assistant to be in that workspace, the needle must be inserted in the grid template. In addition, the maximal translational velocity of the ultrasound probe is limited to 20 mm sec^{-1}.

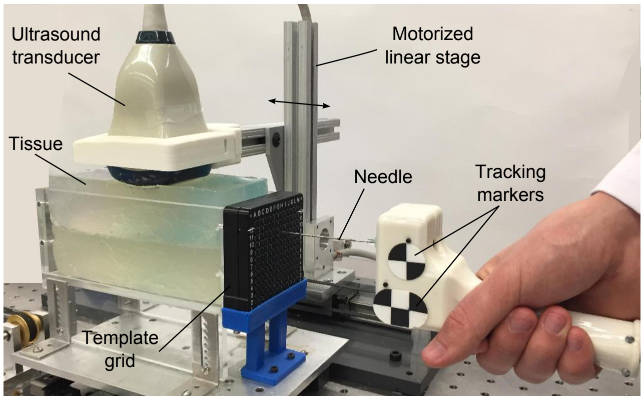

(a) Experimental setup

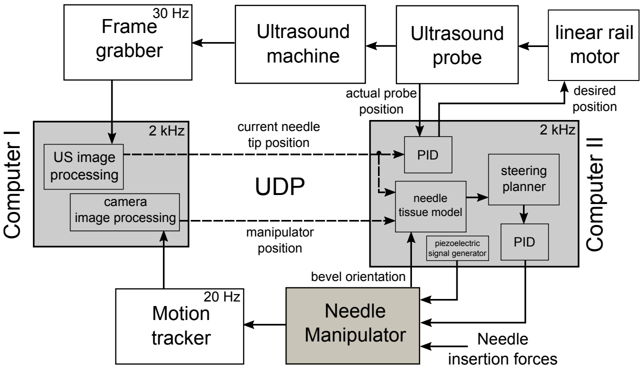

(b) Workflow

Fig. 7. Experimental setup (a) used to validate the proposed system in phantom and *ex-vivo* biological tissue. The needle is inserted into tissue through a grid template. Tracking markers are added to the hand-held apparatus to measure its position in 3D. An ultrasound probe follows the tracking markers to acquire transverse images of the needle as it is inserted. (b) shows the hardware implementation. Two computers communicating via UDP are used. The first computer runs the image processing routines and the second computer controls the hand-held apparatus.

Two computers running Matlab in xPC real-time mode are used in the experimental setup as depicted in Fig. 7(b). Computer I receives images generated by the ultrasound machine which are captured by a frame grabber, and images of the tracking markers obtained by the motion tracker. After processing the images, the measured needle tip deflection in the current ultrasound image and the 3D coordinates of the hand held apparatus are sent via UDP to Computer II, where the current needle tip position feeds the needle-tissue model and the steering algorithm. A PID compensator controls the desired orientation of the needle bevel angle calculated by the steering algorithm. The position of the hand-held assistant is sent to a second digital PID controller that adjusts the horizontal position of the ultrasound imaging plane. Both control loops run at 2000 Hz and the communication delay between them is 4 ms.

We performed needle insertion in three different tissues. Tissue 1 and Tissue 2 are made of industrial gelatin derived from acid-cured tissue (gel strength 300 from Sigma-Aldrich Corporation, Saint Louis, USA). The mass ratio of gelatin to water in Tissue 1 and Tissue 2 is 0.15:1 and 0.2:1, respectively, making Tissue 2 stiffer than Tissue 1. Tissue 3 is prepared by embedding a 130 mm long piece of beef tenderloin in the same gelatin used in Tissue 2. This tissue presents several layers of fat and muscle, making it highly heterogeneous. The gelatin is meant to create a flat surface to ensure good acoustic contact between the ultrasound probe and the biological tissue and to generate a second thin tissue layer. In the experiments in Tissue 3, the needle first goes through the biological tissue and reaches the gelatin layer after 130 mm.

For each of the three tissue samples and two steering cases, we carried out needle insertions to attain two different target depths i.e., 130 mm and 150 mm. This amounts to a total of 12 different experimental scenarios. For each scenario, 6 needle insertions were performed, which yields a total of 72 needle insertions.

VI. EXPERIMENTAL EVALUATION

This section is divided in three parts. First, we will see the effects of longitudinal micro vibrations applied by the piezoelectric actuator on needle-tissue friction. Next, image-based identification of needle tissue interaction model parameters is described. The obtained results are used in the needle steering controller to guide the needle towards the targets.

A. *Effects of Longitudinal Needle Vibration*

In order to observe the effects of needle longitudinal vibration on the needle-tissue frictional forces, the piezoelectric actuator unit connected to a 18-gauge brachytherapy needle is attached to the needle insertion robot presented in [19]. The robot is controlled to insert the needle at a constant insertion velocity of 5 mm s^{-1} through two 40 mm thick tissue samples, one made of plastisol gel (M-F Manufacturing Co., Fort Worth, USA) with a Young's modulus of 25 kPa, and one made of biological tissue. Once the needle tip is placed close the tissue surface, the robot moves the needle towards the tissue by 70 mm, while the axial insertion force is recorded by a force sensor.

As the needle tip passes through the tissue, the measured force corresponds to the axial needle-tissue cutting force plus the frictional force generated along the shaft. Inertial effects are neglected since the needle is driven at a constant velocity. When the needle tip exits the tissue, the measured force corresponds to friction only. In order to observe the effects of the frequency of vibration on the insertion force, for each insertion in plastisol the piezoelectric actuator receives a 5 V in amplitude sinusoidal voltage with frequencies ranging from 0 Hz (no vibration) to 1200 Hz in 200 Hz increments. The measured insertion force for each frequency is presented in Fig. 8(a). The results show that the needle insertion forces are reduced by 48% at 1200 Hz. No considerable variation in the insertion force is observed for frequencies beyond 1200 Hz.

To demonstrate the effects of the amplitude of the longitudinal vibrations on needle-tissue friction, voltages of 0 V (no vibration), 10, 20, 30 and 40 V with a fixed frequency of 100 Hz are applied to the piezoelectric actuator during insertion in the biological tissue sample. For each voltage, the needle is inserted 10 times in tissue. The average needle-tissue friction coefficient measured when the needle tip exits the tissue for each insertion is shown the first panel of Fig. 8(b). At 40 V, the friction coefficient drops by 35% compared to the insertion without vibration.

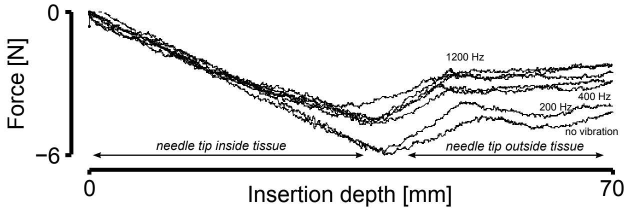

(a) Axial needle insertion force in plastisol

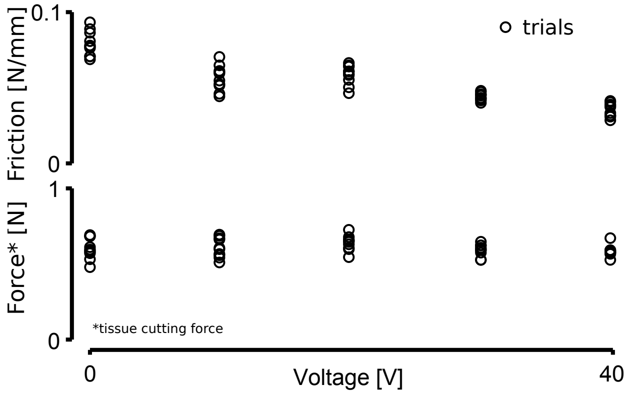

(b) Friction coefficient and tip cutting force in biological tissue

Fig. 8. Effects on vibration on friction forces. In (a) the measured needle-tissue axial insertion force in plastisol for different vibration frequencies is presented. The results show that the forces are reduced by 48% at 1200 Hz. In (b), the needle-tissue friction and cutting force are shown for different voltages with a fixed frequency of 100 Hz.

Knowing the friction coefficient, one can isolate the needle-tissue cutting force $\bar{F}$ applied at the needle tip from the total force measured during tissue cutting [19]. The results shown in the second panel of Fig. 8(b) indicate that the vibration does not lead to significant changes in the measured cutting force. Consequently, and given that the cutting force is the main factor that influences the amount of needle deflection [31], the effects of vibration on the needle deflection are negligible. Since the longitudinal micro-vibrations only reduce the friction component of the insertion force, the user will still experience the force feedback during needle penetration in tissue and also during transitions through different layers.

B. *Model Identification from Ultrasound Images*

To determine the model parameters, i.e., the tip force F and the needle tissue stiffness K that are necessary in the needle-tissue interaction model, three insertions are performed in each tissue without axial needle rotation. From the acquired data, and using the needle-tissue interaction model, these parameters can be calculated. Next, the optimal depths of rotation can be calculated for each experimental scenario as described in Section IV. The model parameters are identified following the 7 steps detailed below.

1) Insert the needle in tissue and record the needle deflection from ultrasound images (see the first plot in Fig. 9);
2) In the needle-tissue model, initialize or, whenever appropriate, update the current needle-tissue stiffness K;

TABLE I
IDENTIFIED MODEL PARAMETERS FOR EACH EXPERIMENTAL SCENARIO

	Gelatin 15%	Gelatin 20%	Biological
Stiffness K [N m^{-2}]	0.5×10^5	1.2×10^5	1.6×10^5
Estimated force F [N]	-0.33	-0.85	-0.73
Measured force $\bar{F}$ [N]	-0.39	-0.96	-0.57

3) Run the observation phase described in Section IV up to 60% of the maximum insertion depth;
4) Calculate the average of the observed force F during the observation phase (see the third panel in Fig. 9. Due to imaging noise, the first 20 mm are not considered);
5) Using the average force F from Step 4 and the current stiffness K from Step 2, run the prediction phase from the end of the observation phase to the maximum insertion depth;
6) Evaluate the mean squared error between the model-predicted and measured needle tip deflection (see the second panel in Fig. 9);
7) Repeat the process from Step 2 until the prediction error in Step 6 reaches a minimum.

Fig. 9 shows the estimated tip deflection for each tissue sample. The prediction error for both phantom tissues is less than 0.2 mm, and increases to 0.5 mm for the biological tissue. The obtained model parameters are summarized in the first two lines of Table I. For comparison, the third line in the table shows the tip force $\bar{F}$ measured for each tissue using the procedure described in Sec. VI-A. Note that different combinations of stiffness K and tip force F can lead to the same tip deflection at a given depth. The disparity between them can be seen in the path followed by the needle tip (i.e., $v_t(d, z)$). Hence, a tissue with high $K - F$ does not necessary have a high Young's modulus, but rather will induce the needle to deflect following a large radius of curvature. This is the case for the biological tissue compared to the gelatin phantoms.

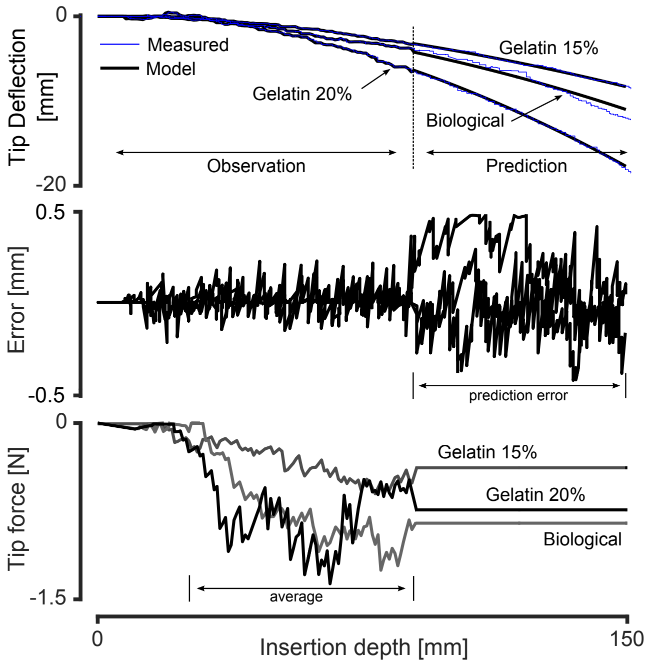

Fig. 9. Model parameters identification for each tissue sample. The first panel shows the measured needle tip deflection and the predicted needle tip deflection using the identified model parameters. The second panel shows the error between the predicted and measured needle tip deflection. The observed tip force is shown in the third panel.

C. Needle Steering

Updating the model parameters as the needle is inserted requires the ultrasound probe to move in synchrony with the needle tip during insertion [32], [33]. However, automated ultrasound probe motion is rarely available in operating rooms. Furthermore, probe motion during brachytherapy can result in additional deformation of the prostate gland [34]. This has been shown to result in anatomic variations of the pre-operatively planned needle targets [35], [36]. Hence, it is desirable to limit the motion of the ultrasound probe. For these reasons, the experiments reported here assume that the identified model parameters are constant during insertion and the steering algorithm does not employ ultrasound images during insertion.

Six needle insertions are performed for each experimental scenario using the hand-held apparatus. Each insertion is done at a new location in tissue to avoid influence of previous insertions on the current one. Table II shows the calculated optimal depth(s) (i.e., d_1, and d_2 if applicable) where the needle rotates by 180 degrees during insertion. As predicted in the simulations reported in Section IV, the higher K the sooner the needle is rotated. The corresponding measured values after insertion of the cost functions J_1 (tip deflection at the target depth d_f) and J_2 (average tip deflection between $d_f - 50$ mm and d_f) are summarized in the sixth and eighth columns of Table 2, respectively.

Note that the objective in Case 1 is to minimize the cost function J_1; J_2 is only presented as an indication of the average tip deflection when the needle approaches the target depth. Likewise, in Case 2, the controller only minimizes J_2. The error between the estimated and measured cost-functions is shown in the last column. For Case 1, this equals J_1. For Case 2 the predicted cost function J_2 is never zero due to the nonholonomic constrains of needle steering. Hence, the reported error is the difference between the model predicted and measured J_2. For Case 1, the average needle tip deflection at the target depth is 0.43 ±0.19 mm. The highest final tip deflection is 0.77 mm, observed for biological tissue, and the lowest is 0.27 mm obtained in the gelatin tissue. With regards to Case 2, the average deflection over the 50 mm preceding the maximum depth is 0.36 ±0.17 mm, and the average prediction error when compared to model predictions is 0.24 mm.

Overall, the average model prediction error over 72 needle insertions is 0.33 ±0.17 mm.

D. Discussion

We have evaluated the ability of the needle steering assistant to minimize needle deflection in two different case studies. The first case intends to minimize the needle tip deflection

TABLE II

MEASURED AVERAGE NEEDLE TIP DEFLECTION (J_1) AT A DEPTH d_f AND AVERAGE NEEDLE TIP DEFLECTION (J_2) BETWEEN d_f AND $d_f - 50$ FOR EACH EXPERIMENTAL CONDITION. ALL UNITS ARE IN MILLIMETRES.

Case	Target depth d_f	Tissue sample	Rotation depth d_1	Rotation depth d_2	Cost function J_1	J_1 stand. deviation	Cost function J_2	J_2 stand. deviation	Prediction error
1	150	Gelatin 15%	59	n.a.	**0.33**	0.38	1.06	0.36	0.33
		Gelatin 20%	56	n.a.	**0.27**	0.28	1.19	0.32	0.27
		Biological	48	n.a.	**0.32**	0.32	0.96	0.48	0.32
	130	Gelatin 15%	53	n.a.	**0.35**	0.39	1.02	0.63	0.35
		Gelatin 20%	50	n.a.	**0.54**	0.21	1.53	0.21	0.54
		Biological	42	n.a.	**0.77**	0.51	0.92	0.37	0.77
-									
2	150	Gelatin 15%	50	138	0.42	0.28	**0.61**	0.53	0.31
		Gelatin 20%	41	123	0.46	0.34	**0.27**	0.54	0.13
		Biological	38	121	0.76	0.31	**0.45**	0.25	0.37
	130	Gelatin 15%	45	122	0.55	0.14	**0.43**	0.50	0.18
		Gelatin 20%	34	110	0.21	0.15	**0.11**	0.14	0.29
		Biological	39	107	0.42	0.25	**0.32**	0.38	0.16
Average of J_1 in Case 1, and J_2 in Case 2					0.43		0.36		
Average over 72 insertions					0.44		0.72		0.33

at the maximum depth (quantified by J_1). The second case minimizes the needle tip deflection over the 50 mm that precede the maximum insertion depth (quantified by J_2). In Case 1 J_1 does not exceed 0.7 mm while J_2 can be as high as 1.19 mm. In Case 2, J_2 is reduced to no more than 0.61 mm without affecting J_1. Hence, it can be concluded that Case 2 also contains Case 1 as a subset, at the cost of only one additional needle rotation.

Deviations from the model predictions are less than 0.77 mm, with an average of 0.33 mm. This can be partially attributed to imaging uncertainties used for model identification and ground truth. Firstly, the ultrasound probe is imaging the needle on average 3 mm behind the needle tip, which in the worst case scenario can induce a deflection measurement error of 0.2 mm. Secondly, the noise present in ultrasound images may impair the ability of the model to capture a small amount of inherent variability in the results and thereby lead to non-negligible variations in the estimated force F.

Another source of uncertainty arises from the operator's susceptibility to involuntarily turn the wrist (rotate) as he/she uses the apparatus. This small rotation of the needle's base can lead to a small change in the angle of the needle bevel tip and can lead the needle to deviate from the predicted path. This can be corrected by measuring the orientation of the device using an inertial measurement unit and rotating the needle axially by the same angle in the opposite direction using the motor inside the device. This issue can also be avoided with specific user training sessions.

In spite of these uncertainties, and with a limited number of model parameters, the proposed system is able to steer a brachytherapy needle towards a desired target with satisfactory accuracy in comparison with other needle-tissue models. For instance, the nonholonomic model [17] reports an error between the model prediction and measurements of 1.3 mm. In [37] the average targeting error during steering is 0.46 mm for different kinematics and mechanics-based models. In [38], a sliding-mode based closed-loop needle steering algorithm has an accuracy of 0.43 mm. Table III shows a comparison of our proposed hand-held apparatus with other reported models and steering algorithms. The prototype also shows fairly good accuracy when compared with fully automated needle insertion systems.

Although the prototype device is meant to reduce the surgeon's workload and perform corrective actions on a measured and calculated basis, the proposed hand-held design still allows the surgeon to perform the usual manual steering manoeuvres such as applying lateral forces to the needle at a point between the grid template and the patient's skin [14]. In addition, corrective actions can be taken automatically by the device, manually by the surgeon, or in combination by both. The needle steering algorithm parameters associated with this device can be entirely identified using only ultrasound images of the needle in tissue. Besides, the device is compact and weighs only 160 grams, making it easy to incorporate with current insertion techniques.

E. Clinical Translation Outlook

The current assistant system employs an abdominal linear ultrasound transducer, which is not designed for prostate brachytherapy. Towards translating the proposed technology into clinical practice, the ultrasound transducer can be replaced with a transrectal ultrasound probe commonly used in brachytherapy. It should be noted that the proposed system requires US images of the needle that can be captured by any 2D ultrasound transducer.

In order to track the needle tip during insertion, the ultrasound probe would follow the needle tip during insertion. For brachytherapy applications, this is only viable as long as the moving parts of the ultrasound probe are not in contact with the surrounding tissue. This could be implemented with a thin, firm sleeve in which a transrectal ultrasound probe translates, such that when the transducer moves, it does not deform the prostate gland and/or adjacent anatomical structures. This feature can be found in some commercially available ultrasound systems such as the TargetScan (Envisioneering Medical, USA) in which the probe is stationary, but the

TABLE III
COMPARISON WITH OTHER DOCUMENTED MODELS (1-2) AND STEERING SYSTEMS (3-7)

		Guidance/ identification	Tissue model	Number of rotations	Targeting error [mm]	Hand-held insertion
Abayazid *et al.*	[37]	US images, ARFI	soft	2-19	0.46	×
Webester *et al.*	[17]	Camera images	stiff	1-2	1.30	×
Rucker *et al.*	[38]	Magnetic tracking	stiff	$\gg 1$	0.43	×
Fichtinger *et al.*	[10]	CT images	soft	2	1.00	×
Schneider *et al.*	[11]	US images	stiff	1	2.50	×
Smith *et al.*	[8]	3D US images	stiff	n.a.	0.27	×
Okazawa *et al.*	[15]	US images	stiff	n.a.	<1.0	✓
Prototype system		US images	soft	1-2	0.44	✓

transverse imaging plane can be translated internally. Another option is the 3D-2052 anorectal ultrasound probe from BK Ultrasound, USA, which translates the axial imaging plane by 60 mm inside the ultrasound probe to construct a 3D volume.

Alternatively, other means of deflection measurement can also be considered, such as force sensor based estimators [39], partial ultrasound image feedback algorithms designed to minimize the ultrasound probe motion [19], or 3D matrix-transducer transrectal ultrasound probes.

Clinical trials will confirm whether the apparent benefits of the proposed system will lead to improvements in brachytherapy efficacy and outcomes. Clinical deployment of the system will require handling issues regarding sterility, accuracy, and risk assessment.

VII. CONCLUSION

This paper addressed the development of a novel needle steering system from design, fabrication and implementation, to validation in *ex-vivo* biological and phantom tissues. The new proposed framework for semi-automated assisted needle insertion is fully hand-held, and *automatically* rotates the needle at optimal rotation depths as the surgeon *manually* inserts it in order to control the needle tip trajectory. The proposed approach relies on a novel design that keeps the surgeon in control of the procedure and requires only minor modifications to the standard brachytherapy procedure.

In addition to the needle steering capabilities, the device can also modulate a vibratory low-amplitude displacement onto the regular insertion profile. As observed in the experimental results, the needle-tissue friction force drops as the frequency or magnitude of the vibration increases. By minimizing frictional effects, soft tissue deformation is reduced [24], which is expected to have a positive impact on seed implantation accuracy. In addition, the microvibrations can allow for easy detection of the needle tip under Doppler ultrasound for image guided needle steering as described in [40], [41], [42].

Expected benefits of the proposed system include more precise needle targeting accuracy for seed placement in brachytherapy and prostate biopsy. For the former, this can result in improved treatment of localized prostate cancer, and motivate new brachytherapy-based treatment solutions in other clinical settings including using brachytherapy for focal treatment of dominant intra-prostatic lesions, where higher radiation doses are needed. Another potential benefit that can result from this system is to make brachytherapy more accessible for inexperienced surgeons or surgeons with lower case volumes, and reduce their current clinical learning curve [43].

Future efforts will focus on quantifying the effects of longitudinal vibrations on seed delivery accuracy and on tracking the final location of seeds to provide at the end of the procedure an accurate map of radiation dosage. Currently, with ultrasound imaging this cannot be done postoperatively with any better than 80% accuracy, but might be improved by tracking seeds as they are placed, given the measurable location of the hand-held device and hence, the predictable deflection of needles.

REFERENCES

[1] Canadian Cancer Society's Steering Committee: Canadian Cancer Statistics 2015. [Online]. Available: http://www.cancer.ca/statistics

[2] American Cancer Society. Prostate Cancer Statistics, 2015. [Online]. Available: http://www.cancer.org/cancer/prostatecancer

[3] M. Keyes et al., "Canadian prostate brachytherapy in 2012," *Canadian Urological Association Journal*, vol. 7, no. 1-2, p. 51, 2013.

[4] R. Taschereau et al., "Seed misplacement and stabilizing needles in transperineal permanent prostate implants," *Radiotherapy and Oncology*, vol. 55, no. 1, pp. 59–63, 2000.

[5] A. Pollack et al., "Preliminary results of a randomized radiotherapy dose-escalation study comparing 70 Gy with 78 Gy for prostate cancer," *Journal of Clinical Oncology*, vol. 18, no. 23, pp. 3904–3911, 2000.

[6] M. Khadem et al., "Ultrasound-guided model predictive control of needle steering in biological tissue," *Journal of Medical Robotics Research*, vol. 01, no. 01, p. 1640007, 2016.

[7] D. Stoianovici et al., "A modular surgical robotic system for image guided percutaneous procedures," in *Medical Image Computing and Computer-Assisted Interventation*. Springer, 1998, pp. 404–410.

[8] W. Smith et al., "Three-dimensional ultrasound-guided core needle breast biopsy," *Ultrasound in Medicine & Biology*, vol. 27, no. 8, pp. 1025–1034, 2001.

[9] J. Cadeddu et al., "Stereotactic mechanical percutaneous renal access," *Journal of Endourology*, vol. 12, no. 2, pp. 121–125, 1998.

[10] G. Fichtinger et al., "System for robotically assisted prostate biopsy and therapy with intraoperative CT guidance," *Academic Radiology*, vol. 9, no. 1, pp. 60–74, 2002.

[11] C. Schneider et al., "A robotic system for transrectal needle insertion into the prostate with integrated ultrasound," in *IEEE International Conference on Robotics and Automation*, 2004, pp. 365–370.

[12] K. Cleary et al., "Image-guided robotic delivery system for precise placement of therapeutic agents," *Journal of Controlled Release*, vol. 74, no. 1, pp. 363–368, 2001.

[13] T. Podder et al., "AAPM and GEC-ESTRO guidelines for image-guided robotic brachytherapy: Report of Task Group 192," *Medical Physics*, vol. 41, no. 10, p. 101501, 2014.

[14] C. Rossa et al., "Multiactuator haptic feedback on the wrist for needle steering guidance in brachytherapy," *IEEE Robotics and Automation Letters*, vol. 1, no. 2, pp. 852–859, July 2016.

[15] S. Okazawa et al., “Hand-held steerable needle device,” *IEEE/ASME Transactions on Mechatronics*, vol. 10, no. 3, pp. 285–296, June 2005.

[16] R. Hendrick et al., “Hand-held transendoscopic robotic manipulators: A transurethral laser prostate surgery case study,” *The International Journal of Robotics Research*, vol. 34, no. 13, pp. 1559–1572, 2015.

[17] R. Webster et al., “Nonholonomic modeling of needle steering,” *The International Journal of Robotics Research*, vol. 25, no. 5-6, pp. 509–525, 2006.

[18] S. Patil et al., “Needle steering in 3D via rapid replanning,” *IEEE Transactions on Robotics*, vol. 30, no. 4, pp. 853–864, 2014.

[19] C. Rossa et al., “Estimating needle tip deflection in biological tissue from a single transverse ultrasound image: application to brachytherapy,” *International Journal of Computer Assisted Radiology and Surgery*, pp. 1–13, 2015.

[20] S. Misra et al., “Mechanics of flexible needles robotically steered through soft tissue,” *The International Journal of Robotics Research*, vol. 29, no. 13, pp. 1640–1660, June 2010.

[21] B. Fallahi et al., “Sliding-based switching control for image-guided needle steering in soft tissue,” *IEEE Robotics and Automation Letters*, vol. 1, no. 2, pp. 860–867, July 2016.

[22] D. Glozman and M. Shoham, “Image-guided robotic flexible needle steering,” *IEEE Transactions on Robotics*, vol. 23, no. 3, pp. 459–467, June 2007.

[23] Z. Neubach and M. Shoham, “Ultrasound-guided robot for flexible needle steering,” *IEEE Transactions on Biomedical Engineering*, vol. 57, no. 4, pp. 799–805, 2010.

[24] I. Khalaji et al., “Analysis of needle-tissue friction during vibration-assisted needle insertion,” in *IEEE/RSJ International Conference on Intelligent Robots and Systems*, Nov 2013, pp. 4099–4104.

[25] G. Genta, *Vibration dynamics and control*. Springer, 2009.

[26] M. Khadem et al., “A two-body rigid/flexible model of needle steering dynamics in soft tissue,” *IEEE/ASME Transactions on Mechatronics*, vol. In press, pp. 1–12, 2016.

[27] C. Rossa et al., “Adaptive quasi-static modelling of needle deflection during steering in soft tissue,” *IEEE Robotics and Automation Letters*, vol. 1, no. 2, pp. 916–923, July 2016.

[28] R. Bhat, “Natural frequencies of rectangular plates using characteristic orthogonal polynomials in Rayleigh-Ritz method,” *Journal of Sound and Vibration*, vol. 102, no. 4, pp. 493–499, 1985.

[29] S. Kirkpatrick et al., “Optimization by simulated annealing,” *Science*, vol. 220, no. 4598, pp. 671–680, 1983.

[30] M. Waine et al., “Needle tracking and deflection prediction for robot-assisted needle insertion using 2D ultrasound images,” *Journal of Medical Robotics Research*, vol. 1, no. 2, pp. 1–11, 2016.

[31] M. Khadem et al., “Mechanics of tissue cutting during needle insertion in biological tissue,” *IEEE Robotics and Automation Letters*, vol. 1, no. 2, pp. 800–807, July 2016.

[32] G. Vrooijink et al., “Needle path planning and steering in a three-dimensional non-static environment using two-dimensional ultrasound images,” *The International Journal of Robotics Research*, pp. 1361–1374, 2014.

[33] M. Abayazid et al., “Experimental evaluation of ultrasound-guided 3D needle steering in biological tissue,” *International Journal of Computer Assisted Radiology and Surgery*, vol. 9, no. 6, pp. 931–939, 2014.

[34] J. Hong et al., “An ultrasound-driven needle-insertion robot for percutaneous cholecystostomy,” *Physics in Medicine and Biology*, vol. 49, no. 3, p. 441, 2004.

[35] M. Lachaine and T. Falco, “Intrafractional prostate motion management with the clarity autoscan system,” *Medical Physics International*, vol. 1, no. 1, pp. 72–80, 2013.

[36] J. Schlosser et al., “Tissue displacement monitoring for prostate and liver IGRT using a robotically controlled ultrasound system,” *Medical Physics*, vol. 38, no. 6, pp. 3812–3812, 2011.

[37] M. Abayazid et al., “Integrating deflection models and image feedback for real-time flexible needle steering,” *IEEE Transactions on Robotics*, vol. 29, no. 2, pp. 542–553, April 2013.

[38] C. Rucker et al., “Sliding mode control of steerable needles,” *IEEE Transactions on Robotics*, vol. 29, no. 5, pp. 1289–1299, 2013.

[39] T. Lehmann et al., “A virtual sensor for needle deflection estimation during soft-tissue needle insertion,” in *IEEE International Conference on Robotics and Automation*, May 2015, pp. 1217–1222.

[40] T. Adebar et al., “3D ultrasound-guided robotic needle steering in biological tissue,” *IEEE Transactions on Biomedical Engineering*, vol. 61, no. 12, pp. 2899–2910, Dec 2014.

[41] R. Feld et al., “Use of needle-vibrating device and color doppler imaging for sonographically guided invasive procedures.” *American Journal of Roentgenology*, vol. 168, no. 1, pp. 255–256, 1997.

[42] M. Fronheiser et al., “Vibrating interventional device detection using real-time 3D color doppler,” *IEEE Transactions on Ultrasonics, Ferroelectrics, and Frequency Control*, vol. 55, no. 6, pp. 1355–1362, 2008.

[43] M. Keyes et al., “Decline in urinary retention incidence in 805 patients after prostate brachytherapy: The effect of learning curve?” *International Journal of Radiation Oncology Biology Physics*, vol. 64, no. 3, pp. 825–834, 2006.

Carlos Rossa received the Engineering and the M.Sc. degrees in Mechatronics from the Ecole Nationale d’Ingénieurs de Metz, France, both in 2010, and earned his Ph.D. degree in robotics from the University of Paris VI, France, in 2013. He is currently a postdoctoral research fellow in the Department of Electrical and Computer Engineering at the University of Alberta, Canada. Dr. Rossa’s research interests involve the design and control of haptic interfaces, actuators and sensors, control engineering, medical robotics, and image-guided surgery.

Nawaid Usmani received his M.D. from McMaster University in 2001. He is currently an Assistant Professor in the Department of Oncology at the University of Alberta. His main research focus is in prostate brachytherapy, which includes quantifying inaccuracies in current brachytherapy techniques, identifying patient populations at a higher risk of toxicity from this treatment, and finding ways to improve outcomes with brachytherapy implants.

Ron Sloboda received his Ph.D. in Nuclear Physics from the University of Alberta in 1979. He is currently a Professor in the Department of Oncology at the University of Alberta. His main research interests are dosimetry and treatment planning for brachytherapy, including the design of clinical studies to obtain patient data that inform model-based dose calculation. His current work is focused on incorporating MRI in the treatment planning, delivery and evaluation processes, particularly for permanent prostate implants and intracavitary cervix treatments.

Mahdi Tavakoli is an Associate Professor in the Department of Electrical and Computer Engineering, University of Alberta, Canada. He received his B.Sc. and M.Sc. degrees in Electrical Engineering from Ferdowsi University and K.N. Toosi University, Iran, in 1996 and 1999, respectively. He received his Ph.D. degree in Electrical and Computer Engineering from the University of Western Ontario, Canada, in 2005. In 2006, he was a post-doctoral researcher at Canadian Surgical Technologies and Advanced Robotics (CSTAR), Canada. In 2007-2008, he was an NSERC Post-Doctoral Fellow at Harvard University, USA. Dr. Tavakoli’s research interests broadly involve the areas of robotics and systems control. Specifically, his research focuses on haptics and teleoperation control, medical robotics and image-guided surgery. Dr. Tavakoli is the lead author of Haptics for Teleoperated Surgical Robotic Systems (World Scientific, 2008).